

Article

Accretion/Ejection Phenomena and Emission-Line Profile (A)symmetries in Type-1 Active Galactic Nuclei

Paola Marziani 

National Institute for Astrophysics (INAF), Astronomical Observatory of Padova, 35122 Padova, Italy; paola.marziani@inaf.it; Tel.: +39-0498293415

Abstract: The distinct behaviors of blue- and redshifted broad emission-line shifts, emitted by ionic species with varying ionization potentials in active galactic nuclei (AGN), can be elucidated by considering the balance between radiation and gravitational forces along the quasar main sequence. Blueshifts are attributed to outflowing motions of the line-emitting gas toward the observer, and they are most pronounced in AGN with high Eddington ratios (Population A) and high luminosities. Conversely, redshifts in the broad-line wings are observed in Balmer emission lines of sources radiating at low Eddington ratios (Population B), though the origin of these redshifts remains a subject of ongoing debate. A correlation linking the redward asymmetry as measured by the centroid shift of the $H\beta$ line profile to the black hole mass lends support to the notion that these shifts arise from gravitational and transverse redshift effects, particularly for black hole masses $M_{\text{BH}} \gtrsim 10^{8.7} M_{\odot}$.

Keywords: active galactic nuclei; optical spectroscopy; ionized gas; broad-line region

1. Introduction

Active galactic nuclei (AGN) are most often characterized by the presence of broad and narrow optical and UV lines emitted by ionic species over a broad range of ionization potential χ . (For introductions to the AGN oriented to optical and UV spectroscopy, see, e.g., [1–3], and the references therein.) Restricting the attention to broad lines, type-1 AGN spectra show the same emission lines [4], although their relative intensity and line profiles can vary greatly from object to object. It is expedient to separate the emission features into two broad groups:

- Low-ionization lines (LILs, ionization potential $\chi_{\text{ion}} \lesssim 20$ eV) that include the lines of the Balmer and Paschen series of Hydrogen, $\text{MgII}\lambda 2800$, the CaII IR Triplet, and FeII features. (UV intermediate-ionization lines (IILs) such as $\text{AlIII}\lambda 1860$, $\text{SiIII}\lambda 1892$, and $\text{CIII}\lambda 1909$ are due to parent species with $15 \lesssim \chi_{\text{ion}} \lesssim 30$ eV that show a behavior similar to the LILs and are frequently associated with them (e.g., [5]).) The most widely studied line is the HI Balmer line $H\beta$.
- High-ionization lines such as $\text{CIV}\lambda 1549$, $\text{HeII}\lambda 1640$, $\text{SiIV}\lambda 1397$, and $\text{NV}\lambda 1240$ (HILs, $\chi_{\text{ion}} \gtrsim 30$ eV) that are strong in rest-frame UV. The most representative feature is the CIV resonant doublet whose parent ionic species has $\chi_{\text{ion}} \approx 54$ eV.

There are substantial differences concerning the broad-line profiles, and inter-line shifts have provided a wealth of information on the kinematics and dynamics as well as on the physical conditions of the line-emitting gas [6–17].

1.1. The (A)symmetric Behavior of Broad Emission Lines

The prototypical HIL CIV may show blueshifts up to several thousand km s^{-1} [18] with respect to the quasar rest frame. (The precise knowledge of the AGN cosmological redshift is a prerequisite for the analysis of the broad-line shifts. Low-ionization emission lines such as $[\text{OII}]\lambda 3727$ and, most often, the narrow component of $H\beta$ ($H\beta_{\text{NC}}$) are used to measure



Citation: Marziani, P.

Accretion/Ejection Phenomena and Emission-Line Profile (A)symmetries in Type-1 Active Galactic Nuclei.

Symmetry **2023**, *15*, 1859. <https://doi.org/10.3390/sym15101859>

Academic Editors: Vittorio De Falco and Daniele Vernieri

Received: 4 September 2023

Revised: 23 September 2023

Accepted: 26 September 2023

Published: 3 October 2023



Copyright: © 2023 by the authors. Licensee MDPI, Basel, Switzerland. This article is an open access article distributed under the terms and conditions of the Creative Commons Attribution (CC BY) license (<https://creativecommons.org/licenses/by/4.0/>).

the systemic redshift [19–21]. Ideally, redshift determination should be based on the host absorption-line spectrum [21] or on the 21 cm line emission of neutral hydrogen. The latter measurements are still limited to nearby AGN and low- z quasars [22–24], although the SKA is expected to extend the redshift limit up to $z \approx 0.8$ for $M_{\text{HI}} \sim 10^{10} M_{\odot}$ (e.g., [25,26]), even at relatively low luminosity ($\log L \gtrsim 44$ [erg s $^{-1}$]). LILs may show prominent asymmetries as well. Figure 1 shows the H β and CIV median profiles overlaid for two classes of type-1 AGN: radio-loud (RL, or relativistically jetted following Padovani et al. [27,28] and Berton et al. [29]), and radio-quiet Population A (RQ, i.e., a population of sources radiating at a high Eddington ratio, Section 1.2). The figure is an updated version of Figure 6 of Marziani et al. [9] that compared the CIV and H β of all the RL vs. all the RQ in their sample and is meant to emphasize a sort of symmetry in the line shifts with respect to the quasar rest frame: whereas HILs show excess blueshifts with respect to LILs, LILs may show an excess redshifted emission. There is a general consensus that blueshifts are due to the Doppler effect associated with outflowing gas approaching the observer (for a dissenting view, see, however, Gaskell [30]). Conversely, the origin of the excess redshift is still debated: the most widely discussed explanations (not mutually exclusive) are infall motions ([31] and the references therein) and gravitational plus transverse redshift (e.g., [32]).

1.2. The Quasar Main Sequence Contextualization

The emission-line relative intensities and their profiles change in a systematic way along the quasar main sequence (the acronym quasar is used here as an interchangeable umbrella term for type-1 AGN). (MS, [6,33,34].) The MS can be represented in a plane where the FWHM H β is diagrammed against the parameter R_{FeII} defined as in the intensity ratio between FeII λ 4570 and the broad component of H β , i.e., $R_{\text{FeII}} = F(\text{FeII}\lambda 4570)/F(\text{H}\beta_{\text{BC}})$. Scatter plots or sketches of the occupation of the quasar MS in this parameter plane have been shown for several large samples (e.g., [33–35]). Here, we recall that Population A, defined by $\text{FWHM}(\text{H}\beta) \lesssim 4000$ km s $^{-1}$, includes Narrow-Line Seyfert 1 galaxies (NLSy1s) and strong FeII emitters. Population B, with $\text{FWHM}(\text{H}\beta) \gtrsim 4000$ kms, is the population to which powerful “jetted” objects usually belong in optically selected, low- z samples [36].

The systematic blueshifts are associated with a high Eddington ratio and reach extreme values if the Eddington ratio is extreme ($L/L_{\text{Edd}} \sim \mathcal{O}(1)$) and the luminosity is very high ($\log L \gtrsim 47$ [erg s $^{-1}$]) [37–39]. Along the MS, this corresponds to the loci of an extreme Population A, with $R_{\text{FeII}} \gtrsim 1$ [40,41]. Redward asymmetries are prominent toward the opposite end of the MS, where FWHM values are large [42], the Eddington ratio is low (Population B, [6]), and the prevalence of a relativistically jetted source is higher [36]. The most extreme redshifts occur for jetted sources [43], although both radio-quiet and radio-loud can show large redward asymmetries, with a considerable overlap [6].

1.3. The Origin of the Redward Shifts

In short, in Population B, we observed a prominent excess toward the red for H β (less so for CIV); in Population A, we observe a symmetric H β profile and a blueshifted CIV. In this note, we focus the attention on the interpretation of the redward asymmetry observed in the broad emission lines. In the next section, we introduce the gravitational redshift and infall motion effects on the broad-line region (Section 2) as possible causes for the broad-line profile excess redshift, in a sample of high mass objects (Section 3). The results (Section 4) indicate that the slope of the line parameters—the black hole mass relation—is more consistent with the gravitational and transverse redshift hypothesis than with the infall. Section 5 summarizes the main luminosity and black hole mass effects on the optical/UV spectra of quasars.

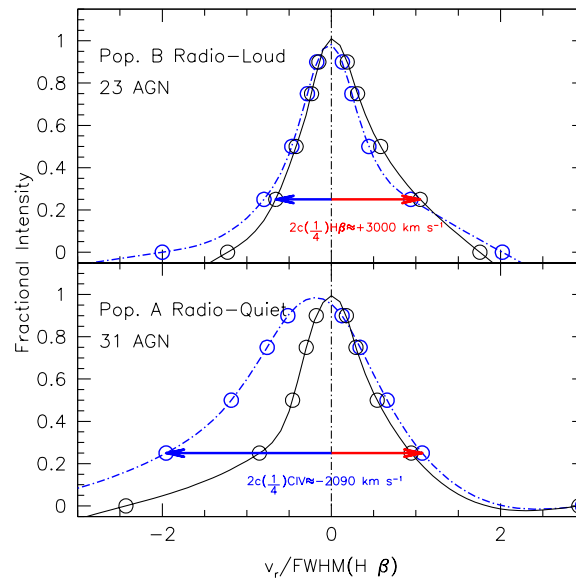


Figure 1. Inter-line comparison between the $H\beta$ (black solid) and $C\text{IV}$ (blue dot-dashed lines) for Pop. B RL (top) and Pop. A RQ (bottom) median composite profiles. The abscissa is radial velocity in km s^{-1} normalized by the FWHM of $H\beta$. The data are from the intersection of the HST/FOS-based sample of Sulentic et al. [18] and of the optical sample of Marziani et al. [44] that includes 83 objects within $z \lesssim 0.75$. The median profiles are computed for Pop. B RL and for Pop. A RQ, the two sub-populations where shifts to the red and to the blue are most extreme. The values twice the $c(\frac{1}{4})$ (defined by Equation (1)) represent the excess width for the blue and red wing of the $C\text{IV}$ and $H\beta$ line profile, respectively.

2. Gravitational Redshift and Infall

2.1. Gravitational Redshift

The hypothesis that redward asymmetry in the emission-line profiles could be due to the gravitational field of the central black hole has been posited since the 1970s [45] and has been reconsidered over time [32,43,46–49]. Perhaps surprisingly, this hypothesis has not gained wide acceptance, even if several lines of evidence are in its favor, as summarized below. (One reason could be that the idea is perceived as “heretic” due to the early attempts to explain the cosmological redshift as gravitational (see the discussion in [50] and Chapter 2 or [51] for historical reports); a second reason is the customary attribution of wavelength shifts to the Doppler effect due to the gas motions. There are alternative processes as shifts due to electron scattering have been proposed [52] but have never been considered for general validity.)

Small size of the line-emitting region—The view of the physical conditions of broad-line-emitting gas has changed considerably in the last decade, thanks especially to the results of reverberation mapping (e.g., [53]). The emitting region radius was found to be a factor of 10 smaller than previously thought [54,55], and its inner radius might be just of the order of a few hundred gravitational radii. The smaller distance of the emitting gas from the central continuum source has important implications for the physical conditions of the gas; the conventional view of the broad-line region (BLR) as a system of emitting clouds characterized by high ionization, typical densities $n_{\text{H}} \sim 10^9 \text{ cm}^{-3}$, and column density $N_{\text{c}} = 10^{23} \text{ cm}^{-2}$ are unable to account for the strong FeII emission in quasars [56,57] observed in Population A (if FeII emission is strong ($R_{\text{FeII}} \gtrsim 0.5$), a high density is needed to maintain the ionization parameter, within reasonable limits; it is now accepted that the bulk of the low-ionization lines requires a high column density, high particle density, low-ionization degree, and high metallicity [58,59]), but it is expected to remain valid for Population B [5].

Inner emitting region radius consistent with the observed shift amplitudes—Estimates of the BLR size are consistent with the emission from several hundred gravitational radii, implying shifts that are $\sim 1000 \text{ km s}^{-1}$.

High prevalence of shifts to the red—They remain ubiquitous in Population B that accounts for 50% of the type-1 AGN in optically selected samples [36, and references therein]. The larger shifts to the red observed for jetted sources are possibly related to their FUV photon deficit that may restrict the illumination of the emitting gas to smaller distances from the central black hole [60,61].

Relativistic accretion disk model fits to low-ionization lines—One of the most impressive feats in the interpretation of AGN line profiles has been the successful modelization of the Balmer line profiles with double peaks in terms of a relativistic accretion disk seen at a moderate orientation [62–64]. The prominent redward asymmetry of the C IV, H β , and Mg II λ 2800 profiles of several blazars has been accounted for by relativistic accretion disk profiles with the disk oriented almost pole-on (disk axis within $\theta \approx 5$ degrees from the line of sight, [43]). The model line profile shows redshifts at the line base consistent with gravitational and transverse redshift, as do the observed profiles.

Shift independent on viewing angle—A corollary of the previous results is that the shifts do not show an obvious dependence on the viewing angle θ : viewing angles cover the full range permitted for unobscured sources $0 \lesssim \theta \lesssim 45$ [65,66].

Full shape of broad profiles—Apart from “double peakers”, the appearance of the H β Population B line profiles, with the shift to the red increasing from the peak toward the line base of the profile, is highly suggestive of a redshift displacement anti-correlated with the distance from the central black hole, $\delta z \propto (r/r_g)^\alpha$.

2.2. Infall

Kinematical models of the BLR based on infall motion have been widely discussed since the early 1980s [67–69]. The recent results of Bao et al. [70] convincingly confirm that the bulk of the line broadening is due to virial velocity fields (as shown in several earlier works, [71–73]), for the objects that meet the selection criterion for Population B. Velocity-resolved reverberation mappings [70,73,74] reveal that the red wing responds with a shorter time delay with respect to the blue one or the line core. This response indicates that the line-emitting gas at extreme positive radial velocities is located closer than the gas emitting the blueshifted emission and suggests infall toward the central black hole. The sub-Keplerian velocity field of an ion torus [75] may lead to systematic infall, but the approaching side of the infalling gas should be somehow obscured to yield a net shift to the red. The approaching part of the inflow, seen from the opposite side of the black hole, might be hidden by the corona, disk atmosphere, and disk wind, or another optically thick structure. By the same token, it is assumed that the receding part of the outflow is not visible to the observer because it is obscured by the optically thick accretion disk. In addition, the maximum inflow velocity may not exceed the local free-fall velocity, unless an improbable force acts to draw the gas toward the black hole. Consequently, the infall hypothesis should be discussed in terms of a net infall radial velocity component lower than the free-fall velocity and associated with the innermost BLR (the shifts amplitudes are larger toward the line base), co-planar or nearly so with the accretion disk.

However, maintaining a radial inflow in the face of a radiation field may not be possible unless the flow is not exposed to the full radiation field, as the radiation field exerts a force that tends to push away any infalling gas. It is anticipated that the inflowing gas will exhibit high turbulence and exhibit chaotic variations in the line profile over relatively short time spans. However, the latter phenomenon is not currently observed. As the innermost BLR is expected to be located at $r \lesssim 1000 R_g$, high cadence monitoring of the line profiles is desirable but not extensively carried out as yet.

2.3. Alternative Scenarios

Supermassive binary black holes (SMBBHs) have been invoked to explain double-peaked profiles or simply asymmetries in the line profiles of quasars [76]. For double peakers, the hypothesis of a binary black hole has been rejected to a high confidence [77,78]. The case of line asymmetries and velocity offsets is apparently more complex, although highly shifted peaks ($\sim 1000 \text{ km s}^{-1}$) usually remain stable in wavelength to the point of requiring exceedingly long periods for the binary. SMBBH models focused on the BLR emission-line profiles suggest that velocity offsets should be present [79]. However, detecting their changes may be less straightforward [80,81]. Given the contribution of a circum-binary disk to the line emission, the profiles should be more stable than in the case of two BLRs, each one rotating around the center of mass of the binary. Periodic phenomena are expected to occur in line and continuum fluxes [81–83], but the computation of velocity-resolved transfer functions from the intrinsic variability in the broad lines is needed for understanding and vetting SMBBH candidates. This requires multi-epoch spectroscopy of large populations of AGN over a variety of time scales [80]. While some candidates are highly suggestive, the lines of evidence summarized in Section 2 argue against the SMBBH being able to explain the high prevalence of redward asymmetries. This said, in a scenario such as the one envisaged by Popović et al. [81], the shift to the red due to gravitation would still be associated with the innermost part of the emitting region bound to the black holes. We might still expect a correlation with mass if SMBBHs were common, but a quantitative prediction would depend on the distribution of the SMBBH mass ratios.

A more intriguing possibility is the presence of a recoiling black hole: an SMBBH formed following a galaxy merger tightens through dynamical processes and eventually coalesces. The anisotropy of the gravitational wave emission in the coalescence process is causing the merged SMBBH to receive a recoil kick [84,85]. One of the most extreme redward asymmetries has been observed in 1E1861+643 [86]. In polarized light, broad lines are found to be blueshifted with blueward asymmetric profiles. These characteristics are explained in terms of a scattering model where the BLR moves away from the observer and toward a scattering region in the host galaxy with a speed of $\sim 2000 \text{ km s}^{-1}$ [87]. Light emitted toward the scattering region is scattered back toward the observer, becomes polarized, and appears blueshifted (as the scattering screen sees the source approaching). The most effective means of confirming the existence of a recoiling black hole is by detecting a displacement relative to the center of mass of the host galaxy. An up-to-date spectroastrometric analysis indicates a spatial displacement of several hundred parsecs for the quasar 1E1861+643 [88]. Nevertheless, it remains unclear how a post-merger gravitational recoil mechanism could be operative within a high-prevalence sample of AGN, as is the case of Pop. B quasars, beyond the explanation of rare extreme shifts (some blueshift $\delta v_r \lesssim -1000 \text{ km s}^{-1}$ are also observed [89]). Special geometries such as the backflow surrounding the radio jet cocoon [90], or even optically thick outflows [91] consistent with the anisotropic emission from the dense gas emitting the broad lines [92], may be applicable only to some peculiar objects as well.

3. Data and Measurements

3.1. Samples

The samples considered for the present analysis are as follows:

Low z ([44], hereafter M03)—The optical sample of Marziani et al. [44] that includes 215 objects within $z \lesssim 0.9$ and with $\log L = 43 - 47$ [erg s^{-1}].

High z (hereafter HEMS)—The 52 sources of the survey of Hamburg ESO quasars at $1 \lesssim z \lesssim 2.6$, where the H β spectral range has been covered by observations obtained with the IR spectrometer ISAAC at VLT (and references therein [48]). These sources are of very high bolometric luminosity $\log L \gtrsim 47$ [erg s^{-1}].

SDSS Low z ([89], hereafter Z10)—This sample is again representative for the luminosity regime $\log L = 43 - 47$ [erg s^{-1}], as vetted to exclude M03 sources. For this last

sample, only the centroid at one-quarter peak intensity (Section 3.2) and the FWHM are available for the analysis.

These samples are preferred over more recent and wider samples because they both involve dedicated fits aimed at a careful extraction of the broad components of CIV and H β from the [OIII] $\lambda\lambda$ 4959,5007 and FeII features that affect the H β broad profile. They have been used as comparison samples for several recent studies addressing the emission-line properties over a very broad range of luminosity (e.g., [93]).

3.2. Measurements

The “asymmetric” behavior concerns the emission-line shifts with respect to the rest frame for the prototypical LIL (H β) and HIL (CIV). The full broad profiles of H β and CIV are parameterized by the FWHM and centroids at a fractional intensity at 1/2 and 1/4 of the peak, $c(\frac{1}{2})$ and $c(\frac{1}{4})$. The definition of centroids can be written as follows [89]:

$$c\left(\frac{i}{4}\right) = \frac{\lambda_B\left(\frac{i}{4}\right) + \lambda_R\left(\frac{i}{4}\right) - 2\lambda_0}{2\lambda_0} c, \quad i = 1, 2, 3; \quad \frac{i}{4} = 0.9 \quad (1)$$

where λ_0 is the laboratory wavelength, and λ_B and λ_R are the wavelengths on the blue and red side of the line at the $i/4$ fractional intensities.

The centroids are referred to the quasar rest frame but are affected by the λ_B that might be, in turn, lowered by blueshifted emission. An alternative to the rest-frame wavelength could be λ_P that may be slightly shifted with respect to the rest frame [7] but not as strongly affected by the blueshifted emission. A proxy to λ_P which will be used in this paper is $\hat{\lambda}_P \approx \lambda_0(1 + c(0.9)/c)$.

For both the [44] and HEMS samples, black hole masses M_{BH} are computed from H β following the recent reformulation from the Sloan reverberation mapping project (that however differs little from the [94] scaling law widely applied in previous studies [95]). A luminosity-dependent bolometric correction $\mathfrak{z}(L)$ [96] from the luminosity at 5100 Å is applied for the Eddington ratio L/L_{Edd} computation.

4. Results

4.1. Relation between H β Broad Wing Redshift and Black Hole Mass for Population B AGN

The $c(\frac{1}{4})$ provides a quantitative measurement of the red excess in the H β broad profile. (The $c(\frac{1}{4})$ should be preferred over the centroid at 0 intensity, $c(\frac{0}{4})$. Even if the latter has a more direct physical meaning, the uncertainties are very large due to the smooth shape of the lines, and the measurement is likely affected by a faint outflowing component that can have a significant effect on the line centroids [97].) The immediate result is a correlation between the two parameters and the black hole mass (Figure 2). The trend is already noted for the data of the HEMS survey [48]; here, the HEMS sample is supplemented by the Pop. B sources of [44]. The correlation is highly significant. For M03 UHEMS, a Pearson’s $r \approx 0.57$ for 101 sources with $c(\frac{1}{4}) > 0 \text{ km s}^{-1}$ has a probability of a chance correlation $p \sim 4 \cdot 10^{-9}$. The scatter is relatively large and may not be due only to the contamination of outflowing gas but also to a large dispersion in the Eddington ratio. The Eddington ratio does not seem to affect the trend: a bivariate analysis implies a dependence on $(0.079 \pm 0.030) \log L/L_{\text{Edd}}$. In addition, the median Eddington ratio $\log L/L_{\text{Edd}} \approx -1.512 \pm 0.625$ is consistent with the typical low values expected for Population B sources, with a dispersion that is roughly correspondent to the measurement uncertainties.

The slope of the best fitting line (unweighted least squares fit) for the M03 UHEMS sample is $a \approx 0.562 \pm 0.086$ (Table 1 presents a summary of the correlation analysis). A consistent value is obtained if a weighted lsq line is used (0.597) or if the Z10 sample is added. The M03 UHEMS lacks Population B sources with masses $\lesssim 10^{8.5} M_{\odot}$. The result from the M03 UHEMS sample is not changed if the reference wavelength is set at the line peak wavelength (middle panel of Figure 2). The right panel of Figure 2 shows the relation for $c(\frac{1}{4}) - c(0.9)$ normalized by the line width at $\frac{1}{4}$: the trend slope is $a \approx 0.2216 \pm 0.0787$.

An application of the bisector method confirms that the slope of the relation $c(\frac{1}{4})-M_{\text{BH}}$ is significantly > 0 .

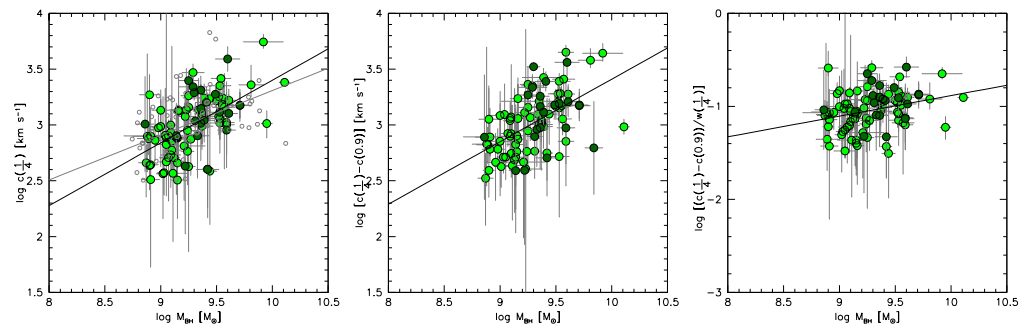


Figure 2. (Left): Correlation between the H β centroid at one-quarter maximum intensity and the black hole mass M_{BH} , for the samples of Marziani et al. [44], M03 (pale green), HEMS (dark green), and Zamfir et al. [89], Z10 (gray open circles). Lines are unweighted least square fits. The gray line refers to the full sample including all samples, while the black line represents a fit performed on HEMS and M03 only. (Middle): Same as left panel, with $c(0.9)$ subtracted to $c(\frac{1}{4})$. (Right): $\delta(\frac{1}{4}) = c(\frac{1}{4})/w(\frac{1}{4})$, i.e., $c(\frac{1}{4}) - c(0.9)$ normalized by the line width at $\frac{1}{4}$ peak intensity. Only shifts above the typical 1σ uncertainty ($\approx 300 \text{ km s}^{-1}$) of $c(\frac{1}{4})$ are considered.

Table 1. Correlation results.

Sample	N	Var.	Pearson ^a		Spearman ^a		LSQ ^b		Bisector ^b	
			r_p	P	r_s	P	a	b	a	b
M03 \cup HEMS	91	$M_{\text{BH}}-c(\frac{1}{4})$	0.571	5×10^{-8}	0.583	6×10^{-10}	0.562 ± 0.086	-2.215 ± 0.795	0.986 ± 0.074	-6.154 ± 0.689
M03 \cup HEMS	89	$M_{\text{BH}}-c(\frac{1}{4})^*$ ^c	0.543	3×10^{-7}	0.569	3×10^{-9}	0.560 ± 0.093	-2.18 ± 0.863	1.025 ± 0.078	-6.518 ± 0.719
M03 \cup HEMS \cup Z10	158	$M_{\text{BH}}-c(\frac{1}{4})$	0.451	1.5×10^{-8}	0.490	1×10^{-10}	0.400 ± 0.063	-0.696 ± 0.589	0.915 ± 0.054	-5.471 ± 0.495
M03 \cup HEMS	89	$M_{\text{BH}}-\delta(\frac{1}{4})$	0.283	0.006	0.311	0.001	0.222 ± 0.079	-3.10 ± 0.731	0.879 ± 0.059	-9.202 ± 0.544

^a: Pearson's and Spearman's correlation coefficients and probability P of chance correlation. ^b: Slope and intercept of shift- M_{BH} correlation in the form $ax + b$. ^c: $c(\frac{1}{4})^* = c(\frac{1}{4}) - c(0.9)$. ^d: $\delta(\frac{1}{4})$ defined as $c(\frac{1}{4})$ normalized by the line width at $\frac{1}{4}$, $\delta(\frac{1}{4}) = c(\frac{1}{4})w(\frac{1}{4})$.

4.2. Interpretation

The main assumption underlying the present analysis is that the velocity field of the emitting region is predominantly virial for the LIL-emitting gas. For the Population B sources, this has been amply verified (e.g., [70,72] and references therein). Nonetheless, the contribution of outflowing gas to the emission lines is ubiquitous in type-1 AGN and may occur on a broad range of spatial scales [98], from a few gravitational radii (e.g., UFOs, [99]) to tens of kiloparsec extended NLRs [38,100]. The ultimate reason why outflows are so ubiquitous relies on a dependence not only on the Eddington ratio and luminosity [37,101] but also on the gas column density [102]: radiation forces may dominate the dynamics of the gas of a sufficiently low column density, leading to outflows on a broad range of spatial scales, from the inner BLR to the NLR. At a low Eddington ratio, and at low L , outflowing gas may not be the dominant contributor to the emission and may have little effect on the measurable broadening and asymmetry parameters, but it is definitely at least perturbing the profiles in the sense that the blueshifted emission is too faint and too heavily blended with the virial component to be accounted for [97]. Therefore, any centroid measurement on the line profile will yield a lower limit to the actual redward displacement associated with gravitational and transverse redshift. The choice of Population B sources and low L/L_{Edd} is meant to minimize the effect of outflowing gas.

A second assumption is the relatively constant physical conditions within the BLR. This is likely the case if the restriction is made to objects belonging to Population B (i.e., showing a prominent redward asymmetry in the Balmer lines) in the innermost part of their emitting regions, the so-called very broad line region (e.g., [103,104]): for the VBLR, the ionization parameter has been estimated as high as $\log U \sim -0.5-0$, with a moderate density $\log n_{\text{H}} \sim 10 \text{ (cm}^{-3}\text{)}$ [5,105], with solar or somewhat subsolar metallicity [105]. These physical conditions have been derived since the late 1970s [106]—before the realization that a large fraction of type-1 AGN emit substantial FeII—and are appropriate for sources that are weak FeII emitters. Concordant properties across Population B are suggested by similar optical and UV spectra indicating a high-ionization condition, with modest FeII and AlIII emissions and prominent CIV [107,108].

Assuming a Keplerian velocity field, the maximum wavelength on the red side of the line corresponds to the maximum projection of the velocity vector along the line of sight [43]:

$$\frac{\lambda_{\text{R}} - \lambda_0}{\lambda_0} = \frac{1}{\sqrt{1 - \beta^2}} \frac{1 + \beta \sin \theta}{\sqrt{1 - 2\beta^2}} \quad (2)$$

where β is the Keplerian velocity normalized by c , $\beta = \sqrt{GM_{\text{BH}}/rc^2}$, and θ is the angle between the line of sight and the accretion disk axes. Note that λ_{R} and λ_{B} may correspond to different fractional intensities along the profile and that there is a one-to-one mapping between $\beta(r)$ measured at different fractional intensities and the emitting region radius right by virtue of the virial velocity field: $\lambda - \lambda_0 \propto \sqrt{M_{\text{BH}}/r}$. Each λ_{R} corresponds to the velocity vector having the maximum projection on the line of sight; for a circular orbit, $v_{\text{r}} = v_{\text{K}} \cos \phi \cdot \sin \theta$, with $\cos \phi = 1$.

If due to gravitational and transverse redshift, the excess on the red side of the line profile can be written as

$$\delta z \approx 2 \cdot c \left(\frac{i}{4} \right) = \frac{\lambda_{\text{R}} - \lambda_0}{\lambda_0} + \frac{\lambda_{\text{B}} - \lambda_0}{\lambda_0} = \frac{1}{\sqrt{1 - \beta^2}} \frac{1}{\sqrt{1 - 2\beta^2}} \approx \frac{3}{2} \beta^2 + \mathcal{O}(\beta^4), \quad (3)$$

and it is independent from the viewing angle. The Taylor expansion is the sum of the gravitational plus the transverse Doppler redshift. The expansion to the second order deviates from the actual shift only by 4 % at $\beta \approx 0.2$ [43].

The gravitational and transverse redshift term can be rewritten as, assuming a bolometric correction dependent on luminosity, $\mathfrak{z} = \mathfrak{z}_0 \left(\frac{L_{5100}}{\Lambda_0} \right)^k$ [96]:

$$\delta z = \frac{3G}{2c^2} \cdot \frac{1}{r_0} \left(\frac{\mathfrak{z}_0}{\Lambda_0^k \mathcal{L}_0} \right)^{\frac{a}{1+k}} \cdot \eta^{\frac{-a}{1+k}} \cdot M^{\frac{1+k-a}{1+k}} \approx 4.7 \cdot 10^{-3} \eta_{0.05}^{-0.625} M_9^{0.375} \quad (4)$$

where $\mathcal{L}_0 = 7.54 \cdot 10^5 \text{ erg s}^{-1} g^{-1}$, and $\Lambda_0 = 10^{42} \text{ erg s}^{-1}$, $k = -0.2$, $\mathfrak{z}_0 = 40$. We have considered that the emitting region radius can be rewritten as $r = r_0 (\eta \mathcal{L}_0 M)^a / \mathfrak{z}^a$, where \mathfrak{z} is the bolometric correction, η is the Eddington ratio, and $a \approx 0.5$ [95,109]. The r_0 value has been set to $\approx 0.25 r_{0,\text{RM}}$, where $r_{0,\text{RM}}$ comes from the most extended reverberation mapping campaign to date [95], and the factor 0.25 comes from the FWHM ratio between the width of the core and of the wing line component. If the bolometric correction is assumed constant, $\mathfrak{z} = 10$, $k = 0$ [110,111]:

$$\delta z \approx \frac{3G}{2c^2} \frac{M \mathfrak{z}^a}{r_0 (\eta \mathcal{L}_0 M)^a} = \frac{3G \mathfrak{z}^a}{2c^2 r_0 \mathcal{L}_0^a} \eta^{-a} M^{1-a} \approx 4.5 \cdot 10^{-3} \eta_{0.05}^{-0.5} M_9^{0.5} \quad (5)$$

The main aspect is that the flux f reaching the BLR is proportional to $1/r^2$, while the amplitude of the gravitational redshift is $1/r$. We expect that

$$\frac{\delta z}{f} \propto \frac{r_{\text{g}}}{r} \cdot \frac{4\pi r^2}{L} \propto r, \quad (6)$$

so increasing as a function of r for the same f (or U). In other words, the flux decreases more rapidly than the gravitational redshift, and therefore the gravitational redshift should increase for the same physical conditions set by f .

The ionization parameter $U(r)$ can be written as

$$U(r) = \frac{Q_H}{4\pi n_H r^2 c} \quad (7)$$

where $Q(H)$ is $Q_H = \int_{\nu_0}^{\infty} L_\nu / h\nu d\nu \approx L_{\text{ion}} / h \langle \nu_{\text{ion}} \rangle$. The ratio Q_H / L_{ion} is uniquely set by the AGN spectral energy distribution. Adopting the Laor et al. [112] continuum appropriate for Population B sources, we have for $L_{\text{ion}} = \kappa L_{\text{bol}}$, $\kappa \approx 0.43$, $\langle h\nu_{\text{ion}} \rangle \approx 2.54$ Ryd. The relation between the redshift and the ionization parameter can be written as

$$\delta z = \frac{6\pi G \langle h\nu_{\text{ion}} \rangle}{c\kappa} \cdot n_H r_0 \left(\frac{\Lambda_0^k}{z_0} \right)^{\frac{a}{1+k}} \mathcal{L}_0^{\frac{a-1-k}{1+k}} \cdot \eta^{\frac{a-1-k}{1+k}} \cdot M^{\frac{a}{1+k}} \cdot U \quad (8)$$

That corresponds to

$$\delta z \sim 10^{-2} n_{H,11} \eta_{0.05}^{-0.375} \cdot M_9^{0.625} \cdot U \quad (9)$$

For $k = -0.2$, the hydrogen density $n_H = 10^{11} \text{ cm}^{-3}$ and $a = 0.5$, appropriate for the $H\beta$ line emission [43]. If the density $n_H \lesssim 10^{10.5} \text{ cm}^{-3}$, the previous relation suggests lower shifts, as it is indeed the case of the very broad component of CIII] [5] whose critical density is $\approx 3 \cdot 10^9 \text{ cm}^{-3}$ [113]. Larger shifts occur if $a \approx 0.533 \gtrsim 0.5$ [95]. Because $\log U \sim -0.5$ – 0 for the VBLR gas of Population B AGN [5,105], there is a good agreement between the amplitude of the redshift and the ionization parameter value at the innermost edge of the BLR.

If we assume that an infall velocity component is added to the Keplerian velocity, i.e., $v_{\text{tot}}^2 = v_K^2 + v_{\text{inf}}^2$, the maximum velocity should be the free-fall velocity, that is, $\sqrt{2}v_K$; in practice, we assume that the infall velocity is κv_K , with $\kappa < \sqrt{2}$. By the same token of Equation (5),

$$c\delta z \approx \kappa \sqrt{\frac{GM}{r}} \sin \theta \approx \kappa \sqrt{\frac{GMz^a}{r_0(\eta L_0 M)^a}} \sin \theta \propto \left(\frac{Gz^a}{r_0 L_0^a} \right)^{\frac{1}{2}} \eta^{-\frac{a}{2}} M^{\frac{1-a}{2}} \quad (10)$$

For $a \approx 0.5$, the dependence on M is stronger for the gravitational redshift case, with $\delta z \propto M^{0.5}$ vs. $\delta z \propto M^{0.25}$. If the shift is normalized by the line width, no trend is expected with the mass in the case of infall, while for the gravitational redshift $\delta z \propto M^{\frac{3a-1}{2}} \propto M^{0.25}$. The observed trends of Figure 2 are in agreement with the prediction for the gravitational redshift, for both M03 UHEMS and [89] with the restriction to $M_{\text{BH}} \gtrsim 10^{8.7} M_\odot$. Lowering minimum shifts to $c(\frac{1}{4}) \gtrsim 10 \text{ km s}^{-1}$ confirms that the trend slopes.

The consideration of lower masses creates a statistically biased sample, as it includes sources of Population B of much lower M_{BH} , down to $\sim 10^6 M_\odot$ whose shift to the red are never above 2σ , the uncertainties. The issue is therefore compounded with the difficulties to measure the centroid close to the line base, with typical uncertainties as high as 300 km s^{-1} (at the 1σ confidence level). The trend would be much shallower and would not rule out the possibility that infall dynamics play a role. However, for masses as low as $\sim 10^7 M_\odot$, following Equation (4), we can expect that the gravitational redshift is rather modest, with $c z$ a few hundred km s^{-1} , and may become again relevant if η tends toward very low values $\lesssim 0.01$. We stress again that Population B sources of the M03 sample at low redshift have large black hole masses, and not only a low Eddington ratio.

5. Discussion

At low z , the picture emerging from the MS is rather straightforward: for moderate luminosity AGN, the main sequence is a sequence of an increasing Eddington ratio, convolved with the effect of orientation [40,59]. The BLR regions are affected by a trend in the ionization parameter, density, and metallicity [59,114]. The Malmquist-type biases of optically selected samples help to shape the MS and make an evolutionary interpretation possible [115]: evolved systems with a high M_{BH} and low L/L_{Edd} , at the one end, and lower M_{BH} and high L/L_{Edd} , edging toward extreme values, at the other end, where prominent FeII emission and overwhelming outflows are observed.

The HEMS Population B quasars—among the most luminous and most massive black holes, in the same extreme luminosity range of the more recent WISSH survey [116]—show very prominent red wings, with several examples shown by Marziani et al. [48] as well as by Vietri et al. [117]. Reaching to the extreme luminosities of the WISSH and HEMS surveys that meet the criterion $L \gtrsim 10^{47} \text{ erg s}^{-1}$, we observe two major effects: (1) an increase in the prominence and velocities of the outflowing components of the HILs [37,117] and (2) an increase in the redward asymmetry of $\text{H}\beta$. The effect (1) is associated with the luminosity-dependent terminal velocity of radiation-driven winds [101] and is mainly a luminosity effect. The effect (2) is associated with the very large black hole masses needed to sustain $L \gtrsim 10^{47} \text{ erg s}^{-1}$. A third effect due to the M_{BH} increase should be added to complete the scenario of high L quasars: (3) the FWHM increase expected right because of the virial velocity field and of the scaling law for the BLR size. The luminosity and M_{BH} dependence is low for effects (1) and (3), $\propto L^{0.25}$, and only becomes significant for large samples with order-of-magnitude spread in luminosity. The gravitational redshift effect can occur at any L , provided that the M_{BH} is sufficiently large and that L/L_{Edd} is sufficiently low (or, in simple terms, that the emitting gas can come close enough to the central black hole). This is confirmed by the samples included in the present analysis.

6. Summary and Conclusions

The distinctive behaviors of broad emission lines—blueshifted and redshifted—emitted by ionic species with varying ionization potentials within AGN find their explication in the equilibrium between radiation and gravitational forces along the quasar MS. Blueshifts, signifying shifts toward shorter wavelengths, arise from outflowing gas motion directed toward observers. These shifts are most conspicuous in AGN boasting high Eddington ratios (Population A along the main sequence) and high luminosities. Conversely, the enigmatic redshifts observed in the broad-line wings emerge in the notable emission lines of sources with low Eddington ratios (Population B) and high black hole masses. The correlation between the specific attributes of the $\text{H}\beta$ line profile, such as redward asymmetry and centroid shift, and the mass of the central black hole buttresses the notion that these shifts could be due to gravitational and transverse redshift effects, especially in cases of black holes exceeding $\approx 10^{8.7}$ solar masses.

Funding: This research received no external funding.

Data Availability Statement: Not applicable.

Acknowledgments: I am thankful to Paola Mazzei for a careful reading of the manuscript.

Conflicts of Interest: The author declares no conflict of interest.

Abbreviations

The following abbreviations are used in this manuscript:

AGN	Active Galactic Nuclei
BLR	Broad-Line Region
FWHM	Full-Width Half-Maximum
HEMS	Hamburg-ESO Marziani and Sulentic
HIL	High-Ionization Line
LIL	Low-Ionization Line
MDPI	Multidisciplinary Digital Publishing Institute
M03	Marziani et al. [44]
MS	Main Sequence
NLR	Narrow-Line Region
NLSy1	Narrow-Line Seyfert 1
PIZ	Partially Ionized Zone
RL	Radio-Loud
RQ	Radio-Quiet
SDSS	Sloan Digital Sky Survey
SMBBH	Supermassive Binary Black Hole
VBLR	Very Broad Line Region
UFO	Ultra Fast Outflow
VBC	Very Broad Component
WISSH	WISE/SDSS-Selected Hyper-luminous
Z10	Zamfir et al. [89]

References

1. Netzer, H. AGN emission lines. In *Active Galactic Nuclei*; Blandford, R.D., Netzer, H., Woltjer, L., Courvoisier, T.J.L., Mayor, M., Eds.; Springer: Berlin/Heidelberg, Germany, 1990; pp. 57–160.
2. Peterson, B.M. *An Introduction to Active Galactic Nuclei*; Cambridge University Press: Cambridge, UK, 1997.
3. Osterbrock, D.E.; Ferland, G.J. *Astrophysics of Gaseous Nebulae and Active Galactic Nuclei*; University Science Books: Mill Valley, CA, USA, 2006.
4. Vanden Berk, D.E.; Richards, G.T.; Bauer, A.; Strauss, M.A.; Schneider, D.P.; Heckman, T.M.; York, D.G.; Hall, P.B.; Fan, X.E.A. Composite Quasar Spectra from the Sloan Digital Sky Survey. *Astron. J.* **2001**, *122*, 549–564.
5. Buendia-Rios, T.M.; Negrete, C.A.; Marziani, P.; Dultzin, D. Statistical analysis of Al III and C III] emission lines as virial black hole mass estimators in quasars. *Astron. Astrophys.* **2023**, *669*, A135.
6. Sulentic, J.W.; Marziani, P.; Dultzin-Hacyan, D. Phenomenology of Broad Emission Lines in Active Galactic Nuclei. *Annu. Rev. Astron. Astrophys.* **2000**, *38*, 521–571. [[CrossRef](#)]
7. Sulentic, J.W. Toward a classification scheme for broad-line profiles in active galactic nuclei. *Astrophys. J.* **1989**, *343*, 54–65. [[CrossRef](#)]
8. Corbin, M.R.; Boroson, T.A. Combined Ultraviolet and Optical Spectra of 48 Low-Redshift QSOs and the Relation of the Continuum and Emission-Line Properties. *Astrophys. J. Suppl.* **1996**, *107*, 69. [[CrossRef](#)]
9. Marziani, P.; Sulentic, J.W.; Dultzin-Hacyan, D.; Calvani, M.; Moles, M. Comparative Analysis of the High- and Low-Ionization Lines in the Broad-Line Region of Active Galactic Nuclei. *Astrophys. J. Suppl. Ser.* **1996**, *104*, 37. [[CrossRef](#)]
10. Richards, G.T.; Vanden Berk, D.E.; Reichard, T.A.; Hall, P.B.; Schneider, D.P.; SubbaRao, M.; Thakar, A.R.; York, D.G. Broad Emission-Line Shifts in Quasars: An Orientation Measure for Radio-Quiet Quasars? *Astron. J.* **2002**, *124*, 1–17. [[CrossRef](#)]
11. Boroson, T. Blueshifted [O III] Emission: Indications of a Dynamic Narrow-Line Region. *Astron. J.* **2005**, *130*, 381–386.
12. Baskin, A.; Laor, A. What controls the CIV line profile in active galactic nuclei? *Mon. Not. R. Astron. Soc.* **2005**, *356*, 1029–1044.
13. Punsly, B. The Redshifted Excess in Quasar C IV Broad Emission Lines. *Astrophys. J.* **2010**, *713*, 232–238.
14. Gaskell, C.M.; Goosmann, R.W. Line Shifts, Broad-line Region Inflow, and the Feeding of Active Galactic Nuclei. *Astrophys. J.* **2013**, *769*, 30.
15. Shen, Y.; Brandt, W.N.; Richards, G.T.; Denney, K.D.; Greene, J.E.; Grier, C.J.; Ho, L.C.; Peterson, B.M.; Petitjean, P.; Schneider, D.P.; et al. The Sloan Digital Sky Survey Reverberation Mapping Project: Velocity Shifts of Quasar Emission Lines. *Astrophys. J.* **2016**, *831*, 7. [[CrossRef](#)]
16. Sun, M.; Xue, Y.; Richards, G.T.; Trump, J.R.; Shen, Y.; Brandt, W.N.; Schneider, D.P. The Sloan Digital Sky Survey Reverberation Mapping Project: The C IV Blueshift, Its Variability, and Its Dependence Upon Quasar Properties. *Astrophys. J.* **2018**, *854*, 128.
17. Ge, X.; Zhao, B.X.; Bian, W.H.; Frederick, G.R. The Blueshift of the C IV Broad Emission Line in QSOs. *Astron. J.* **2019**, *157*, 148.
18. Sulentic, J.W.; Bachev, R.; Marziani, P.; Negrete, C.A.; Dultzin, D. C IV $\lambda 1549$ as an Eigenvector 1 Parameter for Active Galactic Nuclei. *Astrophys. J.* **2007**, *666*, 757–777. [[CrossRef](#)]

19. Eracleous, M.; Halpern, J.P. Accurate Redshifts and Classifications for 110 Radio-Loud Active Galactic Nuclei. *Astrophys. J. Suppl.* **2004**, *150*, 181–186. [[CrossRef](#)]
20. Hu, C.; Wang, J.M.; Ho, L.C.; Chen, Y.M.; Zhang, H.T.; Bian, W.H.; Xue, S.J. A Systematic Analysis of Fe II Emission in Quasars: Evidence for Inflow to the Central Black Hole. *Astrophys. J.* **2008**, *687*, 78–96. [[CrossRef](#)]
21. Bon, N.; Marziani, P.; Bon, E.; Negrete, C.A.; Dultzin, D.; del Olmo, A.; D’Onofrio, M.; Martínez-Aldama, M.L. Selection of highly-accreting quasars. Spectral properties of Fe II_{opt} emitters not belonging to extreme Population A. *Astron. Astrophys.* **2020**, *635*, A151. [[CrossRef](#)]
22. Condon, J.J.; Gower, A.C.; Hutchings, J.B. Radio-Continuum Emission from Quasar Host Galaxies. *Astron. J.* **1987**, *93*, 255. [[CrossRef](#)]
23. Ho, L.C.; Darling, J.; Greene, J.E. A New H I Survey of Active Galaxies. *Astrophys. J. Suppl.* **2008**, *177*, 103–130. [[CrossRef](#)]
24. Robinson, J.H.; Bentz, M.C.; Johnson, M.C.; Courtois, H.M.; Ou-Yang, B. H I Spectroscopy of Reverberation-mapped Active Galactic Nuclei. *Astrophys. J.* **2019**, *880*, 68. [[CrossRef](#)]
25. Obreschkow, D.; Klöckner, H.R.; Heywood, I.; Levrier, F.; Rawlings, S. A Virtual Sky with Extragalactic H I and CO Lines for the Square Kilometre Array and the Atacama Large Millimeter/Submillimeter Array. *Astrophys. J.* **2009**, *703*, 1890–1903. [[CrossRef](#)]
26. Blyth, S.; van der Hulst, T.M.; Verheijen, M.A.W.; Catinella, B.; Fraternali, F.; Haynes, M.P.; Hess, K.M.; Koribalski, B.; Lagos, C.; Meyer, M.; et al. Exploring Neutral Hydrogen and Galaxy Evolution with the SKA. In Proceedings of the Advancing Astrophysics with the Square Kilometre Array (AASKA14), Messina, Italy, 9–13 June 2014 ; p. 128. [[CrossRef](#)]
27. Padovani, P.; Alexander, D.M.; Assef, R.J.; De Marco, B.; Giommi, P.; Hickox, R.C.; Richards, G.T.; Smolčić, V.; Hatziminaoglou, E.; Mainieri, V.; et al. Active galactic nuclei: What’s in a name? *Astron. Astrophys. Rev.* **2017**, *25*, 2. [[CrossRef](#)]
28. Padovani, P. Active Galactic Nuclei at All Wavelengths and from All Angles. *Front. Astron. Space Sci.* **2017**, *4*, 35. [[CrossRef](#)]
29. Berton, M.; Foschini, L.; Caccianiga, A.; Ciroi, S.; Congiu, E.; Cracco, V.; Frezzato, M.; La Mura, G.; Rafanelli, P. An orientation-based unification of young jetted active galactic nuclei: The case of 3C 286. *Front. Astron. Space Sci.* **2017**, *4*, 8. [[CrossRef](#)]
30. Gaskell, C.M. What broad emission lines tell us about how active galactic nuclei work. *New Astron. Rev.* **2009**, *53*, 140–148. [[CrossRef](#)]
31. Wang, J.M.; Du, P.; Brotherton, M.S.; Hu, C.; Songsheng, Y.Y.; Li, Y.R.; Shi, Y.; Zhang, Z.X. Tidally disrupted dusty clumps as the origin of broad emission lines in active galactic nuclei. *Nat. Astron.* **2017**, *1*, 775–783. [[CrossRef](#)]
32. Bon, N.; Bon, E.; Marziani, P.; Jovanović, P. Gravitational redshift of emission lines in the AGN spectra. *Astrophys. Space Sci.* **2015**, *360*, 7. [[CrossRef](#)]
33. Boroson, T.A.; Green, R.F. The Emission-Line Properties of Low-Redshift Quasi-stellar Objects. *Astrophys. J. Suppl.* **1992**, *80*, 109. [[CrossRef](#)]
34. Shen, Y.; Ho, L.C. The diversity of quasars unified by accretion and orientation. *Nature* **2014**, *513*, 210–213. [[CrossRef](#)]
35. Gaskell, C.M. Galactic mergers, starburst galaxies, quasar activity and massive binary black holes. *Nature* **1985**, *315*, 386. [[CrossRef](#)]
36. Ganci, V.; Marziani, P.; D’Onofrio, M.; del Olmo, A.; Bon, E.; Bon, N.; Negrete, C.A. Radio loudness along the quasar main sequence. *Astron. Astrophys.* **2019**, *630*, A110. [[CrossRef](#)]
37. Sulentic, J.W.; del Olmo, A.; Marziani, P.; Martínez-Carballo, M.A.; D’Onofrio, M.; Dultzin, D.; Perea, J.; Martínez-Aldama, M.L.; Negrete, C.A.; Stirpe, G.M.; et al. What does CIV λ 1549 tell us about the physical driver of the Eigenvector quasar sequence? *Astron. Astrophys.* **2017**, *608*, A122. [[CrossRef](#)]
38. Vietri, G. The LBT/WISSH Quasar Survey: Revealing Powerful Winds in the Most Luminous AGN. In *American Astronomical Society Meeting Abstracts*; 2017, Volume 229, pp. 302–306. Available online: <https://ui.adsabs.harvard.edu/abs/2017AAS...22930206V/abstract> (accessed on 1 January 2019)
39. Vietri, G.; Mainieri, V.; Kakkad, D.; Netzer, H.; Perna, M.; Circosta, C.; Harrison, C.M.; Zappacosta, L.; Husemann, B.; Padovani, P.; et al. SUPER. III. Broad line region properties of AGNs at $z \sim 2$. *Astron. Astrophys.* **2020**, *644*, A175. [[CrossRef](#)]
40. Sun, J.; Shen, Y. Dissecting the Quasar Main Sequence: Insight from Host Galaxy Properties. *Astrophys. J. Lett.* **2015**, *804*, L15. [[CrossRef](#)]
41. Du, P.; Lu, K.X.; Hu, C.; Qiu, J.; Li, Y.R.; Huang, Y.K.; Wang, F.; Bai, J.M.; Bian, W.H.; Yuan, Y.F.; et al. Supermassive Black Holes with High Accretion Rates in Active Galactic Nuclei. VI. Velocity-resolved Reverberation Mapping of the H β Line. *Astrophys. J.* **2016**, *820*, 27. [[CrossRef](#)]
42. Wolf, J.; Salvato, M.; Coffey, D.; Merloni, A.; Buchner, J.; Arcodia, R.; Baron, D.; Carrera, F.J.; Comparat, J.; Schneider, D.P.; et al. Exploring the diversity of Type 1 active galactic nuclei identified in SDSS-IV/SPIDERS. *Mon. Not. R. Astron. Soc.* **2020**, *492*, 3580–3601. [[CrossRef](#)]
43. Punsly, B.; Marziani, P.; Berton, M.; Kharb, P. The Extreme Red Excess in Blazar Ultraviolet Broad Emission Lines. *Astrophys. J.* **2020**, *903*, 44. [[CrossRef](#)]
44. Marziani, P.; Sulentic, J.W.; Zamanov, R.; Calvani, M.; Dultzin-Hacyan, D.; Bachev, R.; Zwitter, T. An Optical Spectroscopic Atlas of Low-Redshift Active Galactic Nuclei. *Astrophys. J. Suppl. Ser.* **2003**, *145*, 199–211. [[CrossRef](#)]
45. Netzer, H. On the profiles of the broad lines in the spectra of QSOs and Seyfert galaxies. *Mon. Not. R. Astron. Soc.* **1977**, *181*, 89P–92P. [[CrossRef](#)]
46. Corbin, M.R. QSO Broad Emission Line Asymmetries: Evidence of Gravitational Redshift? *Astrophys. J.* **1995**, *447*, 496. [[CrossRef](#)]

47. Popovic, L.C.; Vince, I.; Atanackovic-Vukmanovic, O.; Kubicela, A. Contribution of gravitational redshift to spectral line profiles of Seyfert galaxies and quasars. *Astron. Astrophys.* **1995**, *293*, 309–314.
48. Marziani, P.; Sulentic, J.W.; Stirpe, G.M.; Zamfir, S.; Calvani, M. VLT/ISAAC spectra of the H β region in intermediate-redshift quasars. III. H β broad-line profile analysis and inferences about BLR structure. *Astron. Astrophys.* **2009**, *495*, 83–112. [[CrossRef](#)]
49. Mediavilla, E.; Jiménez-Vicente, J.; Fian, C.; Muñoz, J.A.; Falco, E.; Motta, V.; Guerras, E. Systematic Redshift of the Fe III UV Lines in Quasars: Measuring Supermassive Black Hole Masses under the Gravitational Redshift Hypothesis. *Astrophys. J.* **2018**, *862*, 104. [[CrossRef](#)]
50. Greenstein, J.L.; Schmidt, M. The Quasi-Stellar Radio Sources 3c 48 and 3c 273. *Astrophys. J.* **1964**, *140*, 1. [[CrossRef](#)]
51. D’Onofrio, M.; Marziani, P.; Sulentic, J.W. (Eds.) *Fifty Years of Quasars from Early Observations and Ideas to Future Research*; Astrophysics and Space Science Library; Springer: Berlin/Heidelberg, Germany, 2012; Volume 386.
52. Laor, A. Evidence for Line Broadening by Electron Scattering in the Broad-Line Region of NGC 4395. *Astrophys. J.* **2006**, *643*, 112–119. [[CrossRef](#)]
53. Marinello, A.O.M.; Rodriguez-Ardila, A.; Garcia-Rissmann, A.; Sigut, T.A.A.; Pradhan, A.K. The FeII emission in active galactic nuclei: Excitation mechanisms and location of the emitting region. *Astrophys. J.* **2016**, *820*, 116. [[CrossRef](#)]
54. Peterson, B.M.; Ferrarese, L.; Gilbert, K.M.; Kaspi, S.; Malkan, M.A.; Maoz, D.; Merritt, D.; Netzer, H.; Onken, C.A.; Pogge, R.W.; et al. Central Masses and Broad-Line Region Sizes of Active Galactic Nuclei. II. A Homogeneous Analysis of a Large Reverberation-Mapping Database. *Astrophys. J.* **2004**, *613*, 682–699. [[CrossRef](#)]
55. Peterson, B.M. Space Telescope and Optical Reverberation Mapping Project: A Leap Forward in Reverberation Mapping. *Proc. Int. Astron. Union* **2017**, *324*, 215–218. [[CrossRef](#)]
56. Collin-Souffrin, S.; Dumont, A.M. Emission spectra of weakly photoionized media in active nuclei of galaxies. *Astron. Astrophys.* **1989**, *213*, 29–48.
57. Collin, S.; Joly, M. The Fe II problem in NLS1s. *New Astron. Rev.* **2000**, *44*, 531–537. [[CrossRef](#)]
58. Panda, S.; Czerny, B.; Adhikari, T.P.; Hryniewicz, K.; Wildy, C.; Kuraszkiwicz, J.; Śniegowska, M. Modeling of the Quasar Main Sequence in the Optical Plane. *Astrophys. J.* **2018**, *866*, 115. [[CrossRef](#)]
59. Panda, S.; Marziani, P.; Czerny, B. The Quasar Main Sequence Explained by the Combination of Eddington Ratio, Metallicity, and Orientation. *Astrophys. J.* **2019**, *882*, 79. [[CrossRef](#)]
60. Punsly, B. The Extreme Ultraviolet Deficit and Magnetically Arrested Accretion in Radio-loud Quasars. *Astrophys. J. Lett.* **2014**, *797*, L33. [[CrossRef](#)]
61. Punsly, B.; Marziani, P.; Kharb, P.; O’Dea, C.P.; Vestergaard, M. The Extreme Ultraviolet Deficit: Jet Connection in the Quasar 1442+101. *Astrophys. J.* **2015**, *812*, 79. [[CrossRef](#)]
62. Chen, K.; Halpern, J.P.; Filippenko, A.V. Kinematic evidence for a relativistic Keplerian disk—ARP 102B. *Astrophys. J.* **1989**, *339*, 742–751. [[CrossRef](#)]
63. Strateva, I.V.; Strauss, M.A.; Hao, L.; Schlegel, D.J.; Hall, P.B.; Gunn, J.E.; Li, L.; Ivezić, V.Z.; Richards, G.T.; Zakamska, N.L.; et al. Double-peaked Low-Ionization Emission Lines in Active Galactic Nuclei. *Astron. J.* **2003**, *126*, 1720–1749. [[CrossRef](#)]
64. Eracleous, M.; Halpern, J.P. Completion of a Survey and Detailed Study of Double-peaked Emission Lines in Radio-loud Active Galactic Nuclei. *Astrophys. J.* **2003**, *599*, 886–908. [[CrossRef](#)]
65. Antonucci, R. Unified models for active galactic nuclei and quasars. *Annu. Rev. Astron. Astrophys.* **1993**, *31*, 473–521. [[CrossRef](#)]
66. Urry, C.M.; Padovani, P. Unified Schemes for Radio-Loud Active Galactic Nuclei. *Publ. Astron. Soc. Pac.* **1995**, *107*, 803. [[CrossRef](#)]
67. Kwan, J.; Carroll, T.J. The kinematics of the broad-line emission gas in quasars and Seyfert nuclei. *Astrophys. J.* **1982**, *261*, 25–29. [[CrossRef](#)]
68. Carroll, T.J.; Kwan, J. Kinematics of the broad-line emission gas in quasars and Seyfert nuclei - Line profiles in a gravitational model. *Astrophys. J.* **1985**, *288*, 73–81. [[CrossRef](#)]
69. Mathews, W.G.; Capriotti, E.R. Structure and dynamics of the broad line region. In *Astrophysics of Active Galaxies and Quasi-Stellar Objects*; Miller, J.S., Ed.; University Science Books: Melville, NY, USA, 1985; pp. 185–233.
70. Bao, D.W.; Brotherton, M.S.; Du, P.; McLane, J.N.; Zastrocky, T.E.; Olson, K.A.; Fang, F.N.; Zhai, S.; Huang, Z.P.; Wang, K.; et al. Monitoring AGNs with H β Asymmetry. III. Long-term Reverberation Mapping Results of 15 Palomar-Green Quasars. *Astrophys. J. Suppl.* **2022**, *262*, 14. [[CrossRef](#)]
71. Peterson, B.M.; Wandel, A. Keplerian Motion of Broad-Line Region Gas as Evidence for Supermassive Black Holes in Active Galactic Nuclei. *Astrophys. J. Lett.* **1999**, *521*, L95–L98. [[CrossRef](#)]
72. Peterson, B.M.; Wandel, A. Evidence for Supermassive Black Holes in Active Galactic Nuclei from Emission-Line Reverberation. *Astrophys. J. Lett.* **2000**, *540*, L13–L16. [[CrossRef](#)]
73. Grier, C.J.; Peterson, B.M.; Horne, K.; Bentz, M.C.; Pogge, R.W.; Denney, K.D.; De Rosa, G.; Martini, P.; Kochanek, C.S.; Zu, Y.; et al. The Structure of the Broad-line Region in Active Galactic Nuclei. I. Reconstructed Velocity-delay Maps. *Astrophys. J.* **2013**, *764*, 47. [[CrossRef](#)]
74. Xiao, M.; Du, P.; Horne, K.; Hu, C.; Li, Y.R.; Huang, Y.K.; Lu, K.X.; Qiu, J.; Wang, F.; Bai, J.; et al. Supermassive Black Holes with High Accretion Rates in Active Galactic Nuclei. VII. Reconstruction of Velocity-delay Maps by the Maximum Entropy Method. *Astrophys. J.* **2018**, *864*, 109. [[CrossRef](#)]
75. Narayan, R.; Yi, I. Advection-dominated Accretion: Underfed Black Holes and Neutron Stars. *Astrophys. J.* **1995**, *452*, 710. [[CrossRef](#)]

76. Halpern, J.P.; Filippenko, A.V. A test of the massive binary black hole hypothesis—ARP 102B. *Nature* **1988**, *331*, 46–48. [[CrossRef](#)]
77. Eracleous, M.; Halpern, J.P.; Gilbert, A.M.; Newman, J.A.; Filippenko, A.V. Rejection of the Binary Broad-Line Region Interpretation of Double-peaked Emission Lines in Three Active Galactic Nuclei. *Astrophys. J.* **1997**, *490*, 216. [[CrossRef](#)]
78. Popović, L.C.; Shapovalova, A.I.; Ilić, D.; Burenkov, A.N.; Chavushyan, V.H.; Kollatschny, W.; Kovačević, A.; Valdés, J.R.; León-Tavares, J.; Bochkarev, N.G.; et al. Spectral optical monitoring of the double-peaked emission line AGN Arp 102B. II. Variability of the broad line properties. *Astron. Astrophys.* **2014**, *572*, A66. [[CrossRef](#)]
79. Popović, L.Č. Super-massive binary black holes and emission lines in active galactic nuclei. *New Astron. Rev.* **2012**, *56*, 74–91. [[CrossRef](#)]
80. Kelley, L.Z. Basic considerations for the observability of kinematically offset binary AGN. *Mon. Not. R. Astron. Soc.* **2021**, *500*, 4065–4077. [[CrossRef](#)]
81. Popović, L.Č.; Simić, S.; Kovačević, A.; Ilić, D. Detecting subparsec supermassive binary black holes: Long-term monitoring perspective. *Mon. Not. R. Astron. Soc.* **2021**, *505*, 5192–5211. [[CrossRef](#)]
82. Nguyen, K.; Bogdanović, T. Emission Signatures from Sub-parsec Binary Supermassive Black Holes. I. Diagnostic Power of Broad Emission Lines. *Astrophys. J.* **2016**, *828*, 68. [[CrossRef](#)]
83. Kovačević, A.B.; Wang, J.M.; Popović, L.Č. Kinematic signatures of reverberation mapping of close binaries of supermassive black holes in active galactic nuclei. III. The case of elliptical orbits. *Astron. Astrophys.* **2020**, *635*, A1. [[CrossRef](#)]
84. Favata, M.; Hughes, S.A.; Holz, D.E. How Black Holes Get Their Kicks: Gravitational Radiation Recoil Revisited. *Astrophys. J. Lett.* **2004**, *607*, L5–L8. [[CrossRef](#)]
85. Merritt, D.; Milosavljević, M. Massive Black Hole Binary Evolution. *Living Rev. Relativ.* **2005**, *8*, 8. [[CrossRef](#)]
86. Shapovalova, A.I.; Popović, L.C.; Chavushyan, V.H.; Burenkov, A.N.; Ilić, D.; Kollatschny, W.; Kovačević, A.; Valdés, J.R.; Patiño-Álvarez, V.; León-Tavares, J.; et al. First Long-term Optical Spectral Monitoring of a Binary Black Hole Candidate E1821+643. I. Variability of Spectral Lines and Continuum. *Astrophys. J. Suppl.* **2016**, *222*, 25. [[CrossRef](#)]
87. Robinson, A.; Young, S.; Axon, D.J.; Kharb, P.; Smith, J.E. Spectropolarimetric Evidence for a Kicked Supermassive Black Hole in the Quasar E1821+643. *Astrophys. J. Lett.* **2010**, *717*, L122–L126. [[CrossRef](#)]
88. Jadhav, Y.; Robinson, A.; Almeyda, T.; Curran, R.; Marconi, A. The spatially offset quasar E1821+643: New evidence for gravitational recoil. *Mon. Not. R. Astron. Soc.* **2021**, *507*, 484–495. [[CrossRef](#)]
89. Zamfir, S.; Sulentic, J.W.; Marziani, P.; Dultzin, D. Detailed characterization of H β emission line profile in low-*z* SDSS quasars. *Mon. Not. R. Astron. Soc.* **2010**, *403*, 1759. [[CrossRef](#)]
90. Norman, C.; Miley, G. Jets and emission-line regions. *Astron. Astrophys.* **1984**, *141*, 85–90.
91. Lawrence, A. Asymmetric Balmer line profiles in Seyfert galaxies. *Nature* **1982**, *295*, 509–510. [[CrossRef](#)]
92. Ferland, G.J.; Peterson, B.M.; Horne, K.; Welsh, W.F.; Nahar, S.N. Anisotropic line emission and the geometry of the broad-line region in active galactic nuclei. *Astrophys. J.* **1992**, *387*, 95–108. [[CrossRef](#)]
93. Deconto-Machado, A.; del Olmo, A.; Marziani, P.; Perea, J.; Stirpe, G.M. High-redshift quasars along the Main Sequence. *arXiv* **2022**, arXiv:2211.03853.
94. Vestergaard, M.; Peterson, B.M. Determining Central Black Hole Masses in Distant Active Galaxies and Quasars. II. Improved Optical and UV Scaling Relationships. *Astrophys. J.* **2006**, *641*, 689–709. [[CrossRef](#)]
95. Shen, Y.; Grier, C.J.; Horne, K.; Stone, Z.; Li, J.I.; Yang, Q.; Homayouni, Y.; Trump, J.R.; Anderson, S.F.; Brandt, W.N.; et al. The Sloan Digital Sky Survey Reverberation Mapping Project: Key Results. *arXiv* **2023**, arXiv:2305.01014. [[CrossRef](#)]
96. Netzer, H. Bolometric correction factors for active galactic nuclei. *Mon. Not. R. Astron. Soc.* **2019**, *488*, 5185–5191. [[CrossRef](#)]
97. Marziani, P.; Deconto-Machado, A.; Del Olmo, A. Isolating an Outflow Component in Single-Epoch Spectra of Quasars. *Galaxies* **2022**, *10*, 54. [[CrossRef](#)]
98. Kudoh, Y.; Wada, K.; Kawakatu, N.; Nomura, M. Multiphase Gas Nature in the Sub-parsec Region of the Active Galactic Nuclei. I. Dynamical Structures of Dusty and Dust-free Outflow. *Astrophys. J.* **2023**, *950*, 72. [[CrossRef](#)]
99. Tombesi, F.; Cappi, M.; Reeves, J.N.; Palumbo, G.G.C.; Yaqoob, T.; Braitto, V.; Dadina, M. Evidence for ultra-fast outflows in radio-quiet AGNs. I. Detection and statistical incidence of Fe K-shell absorption lines. *Astron. Astrophys.* **2010**, *521*, A57. [[CrossRef](#)]
100. Kakkad, D.; Mainieri, V.; Vietri, G.; Carniani, S.; Harrison, C.M.; Perna, M.; Scholtz, J.; Circosta, C.; Cresci, G.; Husemann, B.; et al. SUPER. II. Spatially resolved ionised gas kinematics and scaling relations in $z \sim 2$ AGN host galaxies. *Astron. Astrophys.* **2020**, *642*, A147. [[CrossRef](#)]
101. Laor, A.; Brandt, W.N. The Luminosity Dependence of Ultraviolet Absorption in Active Galactic Nuclei. *Astrophys. J.* **2002**, *569*, 641–654. [[CrossRef](#)]
102. Netzer, H.; Marziani, P. The Effect of Radiation Pressure on Emission-line Profiles and Black Hole Mass Determination in Active Galactic Nuclei. *Astrophys. J.* **2010**, *724*, 318–328. [[CrossRef](#)]
103. Peterson, B.M.; Ferland, G.J. An accretion event in the Seyfert galaxy NGC 5548. *Nature* **1986**, *324*, 345–347. [[CrossRef](#)]
104. Snedden, S.A.; Gaskell, C.M. The Case for Optically Thick High-Velocity Broad-Line Region Gas in Active Galactic Nuclei. *Astrophys. J.* **2007**, *669*, 126–134. [[CrossRef](#)]
105. Marziani, P.; Panda, S.; Deconto Machado, A.; Del Olmo, A. Metal Content in Relativistically Jetted and Radio-Quiet Quasars in the Main Sequence Context. *Galaxies* **2023**, *11*, 52. [[CrossRef](#)]
106. Davidson, K.; Netzer, H. The emission lines of quasars and similar objects. *Rev. Mod. Phys.* **1979**, *51*, 715–766. [[CrossRef](#)]

107. Bachev, R.; Marziani, P.; Sulentic, J.W.; Zamanov, R.; Calvani, M.; Dultzin-Hacyan, D. Average Ultraviolet Quasar Spectra in the Context of Eigenvector 1: A Baldwin Effect Governed by the Eddington Ratio? *Astrophys. J.* **2004**, *617*, 171–183. [[CrossRef](#)]
108. Kuraszkiewicz, J.; Wilkes, B.J.; Schmidt, G.; Smith, P.S.; Cutri, R.; Czerny, B. Principal Component Analysis of the Spectral Energy Distribution and Emission Line Properties of Red 2MASS Active Galactic Nuclei. *Astrophys. J.* **2009**, *692*, 1180–1189. [[CrossRef](#)]
109. Bentz, M.C.; Denney, K.D.; Grier, C.J.; Barth, A.J.; Peterson, B.M.; Vestergaard, M.; Bennert, V.N.; Canalizo, G.; De Rosa, G.; Filippenko, A.V.; et al. The Low-luminosity End of the Radius-Luminosity Relationship for Active Galactic Nuclei. *Astrophys. J.* **2013**, *767*, 149. [[CrossRef](#)]
110. Elvis, M.; Wilkes, B.J.; McDowell, J.C.; Green, R.F.; Bechtold, J.; Willner, S.P.; Oey, M.S.; Polomski, E.; Cutri, R. Atlas of quasar energy distributions. *Astrophys. J. Suppl.* **1994**, *95*, 1–68. [[CrossRef](#)]
111. Richards, G.T.; Lacy, M.; Storrie-Lombardi, L.J.; Hall, P.B.; Gallagher, S.C.; Hines, D.C.; Fan, X.; Papovich, C.; Vanden Berk, D.E.; Trammell, G.B.; et al. Spectral Energy Distributions and Multiwavelength Selection of Type 1 Quasars. *Astrophys. J. Suppl.* **2006**, *166*, 470–497. [[CrossRef](#)]
112. Laor, A.; Jannuzi, B.T.; Green, R.F.; Boroson, T.A. The Ultraviolet Properties of the Narrow-Line Quasar I ZW 1. *Astrophys. J.* **1997**, *489*, 656. [[CrossRef](#)]
113. Zheng, W. The Critical Densities for Some Emission Lines. *Astrophys. Lett. Commun.* **1988**, *27*, 275.
114. Marziani, P.; Sulentic, J.W.; Negrete, C.A.; Dultzin, D.; Zamfir, S.; Bachev, R. Broad-line region physical conditions along the quasar eigenvector 1 sequence. *Mon. Not. R. Astron. Soc.* **2010**, *409*, 1033–1048. [[CrossRef](#)]
115. Fraix-Burnet, D.; Marziani, P.; D’Onofrio, M.; Dultzin, D. The Phylogeny of Quasars and the Ontogeny of Their Central Black Holes. *Front. Astron. Space Sci.* **2017**, *4*, 1. [[CrossRef](#)]
116. Bischetti, M.; Piconcelli, E.; Vietri, G.; Bongiorno, A.; Fiore, F.; Sani, E.; Marconi, A.; Duras, F.; Zappacosta, L.; Brusa, M.; et al. The WISSH quasars project. I. Powerful ionised outflows in hyper-luminous quasars. *Astron. Astrophys.* **2017**, *598*, A122. [[CrossRef](#)]
117. Vietri, G.; Piconcelli, E.; Bischetti, M.; Duras, F.; Martocchia, S.; Bongiorno, A.; Marconi, A.; Zappacosta, L.; Bisogni, S.; Bruni, G.; et al. The WISSH quasars project. IV. Broad line region versus kiloparsec-scale winds. *Astron. Astrophys.* **2018**, *617*, A81. [[CrossRef](#)]

Disclaimer/Publisher’s Note: The statements, opinions and data contained in all publications are solely those of the individual author(s) and contributor(s) and not of MDPI and/or the editor(s). MDPI and/or the editor(s) disclaim responsibility for any injury to people or property resulting from any ideas, methods, instructions or products referred to in the content.